ADVANCED FUNCTIONAL MATERIALS
www.afm-journal.de

Organic Hybrid Perovskite ($MAPbI_{3-x}Cl_x$) for Thermochromic Smart Window with Strong Optical Regulation Ability, Low Transition Temperature, and Narrow Hysteresis Width

Sai Liu, Yu Wei Du, Chi Yan Tso, Hau Him Lee, Rui Cheng, Shien-Ping Feng, and Kin Man Yu*

Recently, organic hybrid halide perovskites have been found to show thermochromism with good optical performance, which can be applied in smart windows to reduce building energy consumption. However, these perovskites have shortcomings regarding their thermochromic performance, namely long transition time, high transition temperature, and large transition hysteresis width. In this study, a hydrated $MAPbI_{3-x}Cl_x$ thermochromic perovskite smart window (H-$MAPbI_{3-x}Cl_x$ TPSW) is proposed, which undergoes a reversible transition between a transparent state and a dark reddish-brown tinted state with a high solar modulation ability of 23.7%. Most importantly, the H-$MAPbI_{3-x}Cl_x$ TPSW possesses a tunable low transition temperature of 29.4 to 51.4 °C, a controllable and narrow transition hysteresis width (7.7–13.2 °C) and a short transition time (1–4 min). Additionally, a mathematical model is developed to predict the transition temperature of the H-$MAPbI_{3-x}Cl_x$ TPSW. A field test is also conducted, demonstrating that the H-$MAPbI_{3-x}Cl_x$ TPSW fitted to a model house can reduce the indoor air temperature by 3.5 °C compared to using a quartz glass window. Overall, the H-$MAPbI_{3-x}Cl_x$ TPSW can yield excellent optical properties, while simultaneously providing remarkable transition properties, making it potentially useful for a wide range of applications in energy-efficient buildings.

1. Introduction

With the rapid development of technology and the economy, energy shortage has become a critical issue in urban cities, and the huge energy consumption by buildings is a main cause.[1] According to the statistics, nearly 60% of building energy is consumed by heating, ventilation, and air conditioning (HVAC) systems to achieve a thermally comfortable environment.[2] The major source of the huge consumption by HVAC systems is recognized as the heat transfer to building envelopes, especially the heat loss/gain through windows that accounts for 50% in a typical office building.[3] To reduce the energy consumption without sacrificing thermal comfort, energy-efficient smart windows are urgently needed, hence the extensive investigation in recent years.[4–8] Smart windows are glazed units coated with special materials having spectral response properties, that enable them to adjust the light transmittance in a dynamic and smart way according to the ambient environment. Normally, smart windows can be categorized as electrochromic, photochromic and thermochromic according to the kind of external stimuli inducing the response of the material.[9] Thermochromic smart windows are competitive because of their automatic passive controllability of solar irradiance, which does not require extra energy input.[10] Notably, for thermochromic smart windows, the high luminous transmittance τ_{lum} (i.e., total transmitted light of materials from wavelength of 380–780 nm) and solar modulation ability $\Delta\tau_{sol}$ (i.e., the difference of solar transmittance τ_{sol} between the cold state and hot state of materials) are the keys to ensuring indoor light intensity as well as the energy saving performance. Meanwhile, transition properties including a reasonable transition temperature (T_c), relatively narrow hysteresis width (ΔT_c) as well as short transition time (t_c) are vital for their practical application. T_c is an important parameter in smart window applications. A T_c ranging from 30 to 40 °C is required in building applications.[10] ΔT_c is another important indicator to examine the thermochromic smart window performance, defined as the difference of T_c between the heating ($T_{c,h}$) and cooling processes ($T_{c,c}$) (i.e., $\Delta T_c = T_{c,h} - T_{c,c}$).[11–14]

In recent years, perovskites, in particular hybrid halide perovskites have become popular materials because of their unique material properties suitable for high efficiency solar

S. Liu, Y. W. Du, Dr. C. Y. Tso, Dr. H. H. Lee
School of Energy and Environment
City University of Hong Kong
Tat Chee Avenue Kowloon Tong, Hong Kong, China
E-mail: chiytso@cityu.edu.hk
Dr. R. Cheng, Dr. S.-P. Feng
Department of Mechanical Engineering
The University of Hong Kong
Pokfulam, Hong Kong, China
Prof. K. M. Yu
Department of Physics
City University of Hong Kong
Tat Chee Avenue Kowloon Tong, Hong Kong, China
The ORCID identification number(s) for the author(s) of this article can be found under https://doi.org/10.1002/adfm.202010426.

DOI: 10.1002/adfm.202010426

cells.[15–22] Furthermore, it has been found that semi-transparent photovoltaics of some halide perovskites with a structure ABX_3 (A = $CH_3NH_3^+$ (MA), $HC(NH_2)_2^+$ (FA), and Cs^+; B=Pb^{2+}, Sn^{2+}; X=I^-, Br^-, and Cl^-) can be developed and applied in power generation windows.[23] Notably, researchers discovered that some halide perovskite materials can also perform reversible color and phase change between low and high temperature, demonstrating their potential for thermochromic smart window applications.[9] J. Lin et al. reported that cesium lead iodide/bromide ($CsPbI_{3-x}Br_x$, $0 \le x \le 3$) perovskite undergoes thermally-driven reversible transitions (T_c of 150 °C) between non-perovskite phase and colored perovskite phase with 81.7% and 35.4% visible transparency, respectively.[24] L. M. Wheeler et al. leveraged low formation and dissociation energy of the methylammonium lead iodide ($MAPbI_3$)-methylamine complex to demonstrate a switchable solar cell between the transparent state (68% visible transmittance) and the opaque state (<3% visible transmittance) with a transition temperature of 35 °C.[25] However, the toxicity and flammability of methylamine may hinder its wide application.[26] M. D. Bastiani et al. synthesized methyl-ammonium iodide/bromide perovskite inks which can reversibly change from yellow at 25 °C to orange at 60 °C by increasing the iodide content in the crystals through an unusual crystallization process.[27] Recently, humidity related chromic perovskite has also been explored. B.A. Rosales et al. discovered a reversible multicolor chromism in layered formamidinium (FA) metal halide perovskites, which is stimulated by solvent vapor and temperature.[28] The dynamic color change can be performed by the transition from 2D FA_2PbX_4 to 3D α-$FAPbX_3$ and 1D δ-$FAPbI_3$. S.K. Sharma et al. studied the reversible dimensionality tuning and chromic behaviors of methylammonium lead halides ($MAPbX_3$) upon exposure to humidity.[29] The dimensionality reduction from 3D to 0D of $MAPbX_3$ leads to the reversible transformation from a colored state to colorless state. With the similar water-related mechanism, Halder et al. found that the color of $MAPbI_3$ can be reversibly tuned during the heating–cooling loop by synthesizing the precursor solution that consisted of 4:1 molar ratio of MAI to PbI_2. They suggested that the thermochromism was attributed to the hydration and dehydration process (Equation (1)):[30]

$$MAPbI_3 + 3MAI \overset{H_2O}{\leftrightarrow} MA_4PbI_6 \cdot 2H_2O \quad (1)$$

At the cold state, the dihydrated perovskite $MA_4PbI_6 \cdot 2H_2O$ is transparent, and at the hot state it becomes opaque because of the existence of organic–inorganic lead halide perovskite $MAPbI_3$. Following that work, Y. Zhang et al. successfully developed a hydrated $MAPbI_3$ (H-$MAPbI_3$) thermochromic perovskite smart window, recording a τ_{lum} of 90% at the cold state, 34.3% at the hot state, and $\Delta\tau_{sol}$ of 25.5%.[31] The high transparency at the cold state and the high $\Delta\tau_{sol}$ of H-$MAPbI_3$ thermochromic perovskite demonstrate it to be a good candidate for thermochromic smart window applications. But, the transition temperature of H-$MAPbI_3$ perovskite thermochromic smart windows is relatively high (>50 °C in the heating process), and this limits its real-life application in buildings since in most places window temperatures normally do not reach 50 °C, even in the summer. In addition, the difference of transition temperature between heating and cooling cycles is large (i.e., larger than 18 °C), implying that the thermochromism of H-$MAPbI_3$ smart windows may suffer from severe transition hysteresis, such as insensitive optical response to temperature. Therefore, these problems must be addressed before the widespread deployment of perovskite thermochromic smart windows in buildings.

Although significant advancements have been reported on the thermochromism of halide perovskites, both the optical properties and transition properties of thermochromic perovskites remain unsatisfactory. Therefore, this work aims to develop a perovskite thermochromic smart window that has good optical properties (high τ_{lum} and $\Delta\tau_{sol}$), lower T_c, narrower ΔT_c and shorter t_c. To achieve these goals, a novel hydrated $MAPbI_{3-x}Cl_x$ (H-$MAPbI_{3-x}Cl_x$) thermochromic perovskite smart window (TPSW) is proposed, which utilizes thermal heating to dissociate H_2O from the $MAPbI_{3-x}Cl_x$ layer, thus transforming from the transparent state to the colored state. And this phenomenon is reversible upon cooling to rebind H_2O. H-$MAPbI_{3-x}Cl_x$ TPSW demonstrates high τ_{lum} and $\Delta\tau_{sol}$ and excellent transition properties. In addition, a thermodynamic mathematic model was developed to predict the T_c of the H-$MAPbI_{3-x}Cl_x$ thermochromic perovskite, providing a convenient way for users to control the T_c of perovskite smart windows according to their needs. Most importantly, a model house field test was conducted in Hong Kong (sub-tropical climate) to examine the feasibility and energy saving performance of the H-$MAPbI_{3-x}Cl_x$ TPSW in practical applications. Overall, the novel H-$MAPbI_{3-x}Cl_x$ thermochromic perovskite proposed in this study is competitive among all the thermochromic perovskites reported for smart window applications, and it shows great potential to reduce the high energy consumption in buildings.

2. Results and Discussion

2.1. Synthesis and Composition Analysis of H-$MAPbI_{3-x}Cl_x$ Thermochromic Perovskite

The H-$MAPbI_{3-x}Cl_x$ thermochromic perovskite was synthetized by the spin coating method using a solution precursor of MAI and $PbCl_2$ in dimethylformamide (DMF) solvent. The precursor was spin-coated on quartz glass substrates, followed by thermal annealing in the glovebox at 100 °C for 60 min (**Figure 1**a). It should be noted that the thermochromism of H-$MAPbI_{3-x}Cl_x$ is attributed to hydration and dehydration, so the reversible color change cannot be observed in the inert environment (glovebox). After the H-$MAPbI_{3-x}Cl_x$ thermochromic perovskite samples were removed from the glovebox to ambient environment, the thermochromism could be observed upon heating and cooling. To identify the proper concentration ratio of MAI and $PbCl_2$ that can achieve remarkable thermochromism, a series of precursor solutions were made with the molar ratio of MAI and $PbCl_2$ varied from 4:1 to 7:1. At the hot state (60 °C), all these samples are dark reddish-brown. As the temperature is reduced, discoloration of the film occurs until it becomes transparent at the cold state (25 °C). However, it is found that only the samples with the relative molar concentration of MAI to $PbCl_2$ higher than 6:1 (i.e., MAI:$PbCl_2$ = 6.5:1 and 7:1) can achieve complete

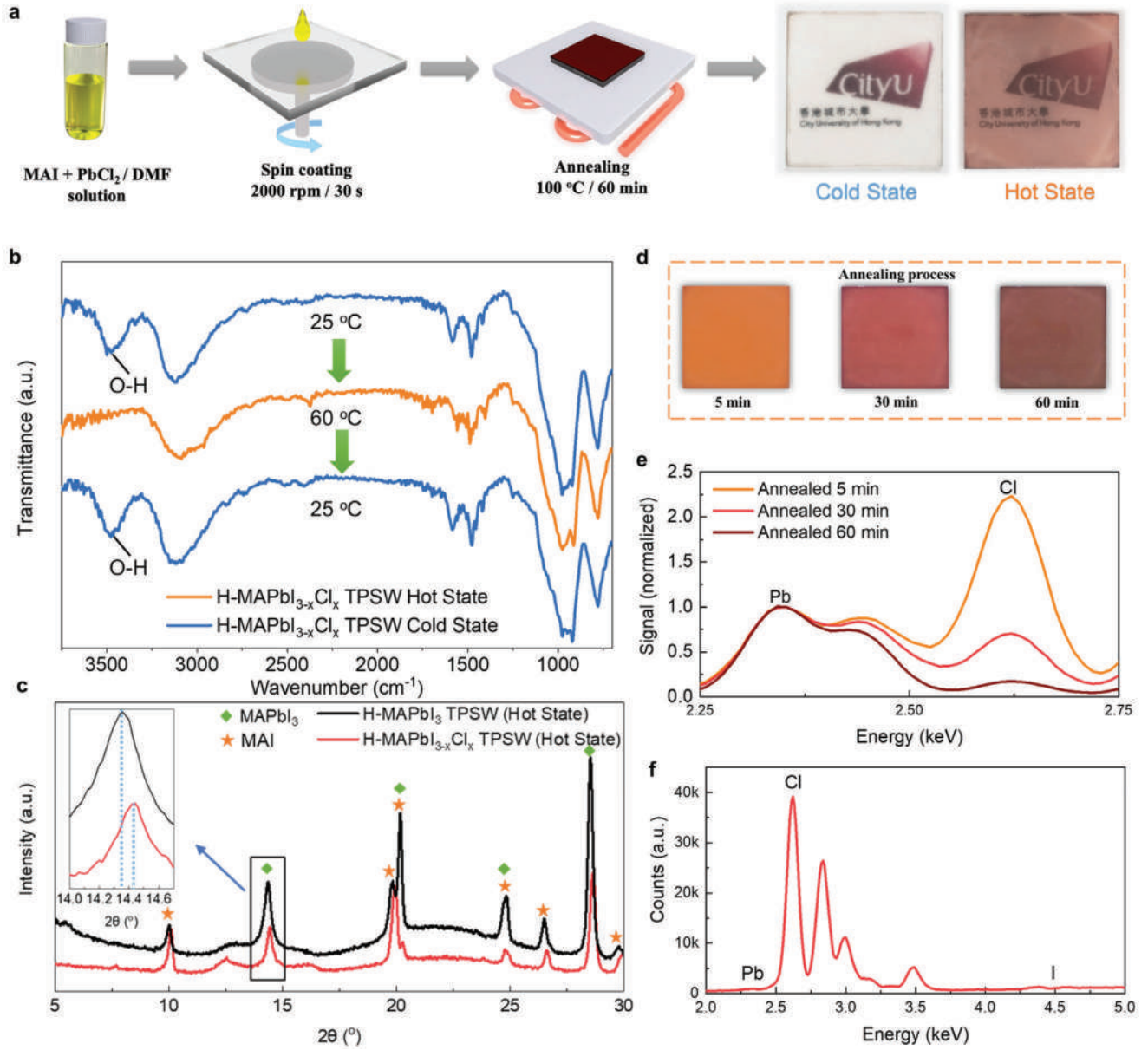

Figure 1. a) Schematics of the fabrication process and photos of H-MAPbI$_{3-x}$Cl$_x$ TPSW at the cold and hot states. b) FTIR spectrum comparison of H-MAPbI$_{3-x}$Cl$_x$ thermochromic perovskite at the cold and hot states. c) XRD patterns of H-MAPbI$_{3-x}$Cl$_x$ and H-MAPbI$_3$ thermochromic perovskite at the hot state as well as the zoom-in pattern from 14° to 14.7°. d) Photos of H-MAPbI$_{3-x}$Cl$_x$ thermochromic perovskite during the annealing process. e) XRF analysis of H-MAPbI$_{3-x}$Cl$_x$ thermochromic perovskite under different annealing times. f) XRF analysis of precipitate on the blank glass attached on the petri dish of Figure S4, Supporting Information.

transparency at the cold state, while other samples appear a dark grey (Figure S1, Supporting Information). X-ray diffraction (XRD) measurements on the sample with 4:1 MAI:PbCl$_2$ ratio at the cold state clearly shows the tetragonal structure of MAPbI$_3$, and yet the intensity of the MAPbI$_3$ characteristic peak decreases with an increase of MAI concentration (Figure S2, Supporting Information). The MAPbI$_3$ characteristic peak completely disappears when the MAI:PbCl$_2$ ratio of the precursor is higher than 6:1. The existence of MAPbI$_3$ perovskite at the cold state leads to the dark grey appearance. At the same time, with the increase of MAI in the precursor, the strong MAI characterization peak can be detected when the MAI:PbI$_2$ ratio reaches 7:1. Notably, for the mixing ratio of 6.5:1, no characterization peak relating to diffractions from the residual MAPbI$_3$ and MAI can be observed, therefore, the mixing ratio of 6.5:1 of MAI and PbCl$_2$ is chosen for further experiment. It should be noted that the reversible thermochromism can also be controlled by the ambient relative humidity (*RH*) without heating/cooling process. Figure S3, Supporting Information exhibits an H-MAPbI$_{3-x}$Cl$_x$ sample which was placed in an environment-controlled chamber with the ambient temperature set at ≈22 °C and the *RH* was modulated from 30% to 10%. The results show

that the sample changed from a transparent state to a reddish-brown state when the *RH* reduced to ≈10%. The modulation of humidity was then reversed (i.e., from 10% to 30%) to perform the humidification process. The reddish-brown started to fade and the sample recovered its transparent state during the increase of *RH* to 30%. This phenomenon indicates that water vapor plays an essential role in the thermochromic process of H-MAPbI$_{3-x}$Cl$_x$.

To investigate the effect of water vapor on the reversible thermochromism, Fourier transform infrared spectroscopy (FTIR) measurements were conducted for the H-MAPbI$_{3-x}$Cl$_x$ thermochromic perovskite. Figure 1b shows the FTIR spectra of the novel H-MAPbI$_{3-x}$Cl$_x$ thermochromic perovskite (synthesized by the precursor of MAI:PbCl$_2$ = 6.5:1) at both the hot state and cold state. It can be seen from the spectrum that a clear signature peak of H—O bond appears at around 3500 cm^{-1} when the perovskite sample is at 25 °C. When the sample is heated to 60 °C, the H—O bond completely disappears, while the other chemical bonds remain the same. The H—O bond appears again when the sample is cooled back to 25 °C. In addition, no color change can be observed in the glove box where the humidity level is low (≤1 ppm). These results not only indicate the existence of condensed water at the clear state of H-MAPbI$_{3-x}$Cl$_x$, but also prove that water functions as the essential driving force in the reversible thermochromism of H-MAPbI$_{3-x}$Cl$_x$ thermochromic perovskite.

Moreover, the measurement of energy dispersive X-ray spectroscopy (EDS) was also conducted for the H-MAPbI$_{3-x}$Cl$_x$ at the cold state, showing the atomic ratio of I:Cl:Pb = 5.98:0.40:1, proving that only a small amount of Cl exists in the H-MAPbI$_{3-x}$Cl$_x$ thermochromic perovskite film, and the atomic ratio of halide element (Cl + I) and lead is 6.38:1, which is close to the previously reported H-MAPbI$_3$ thermochromic perovskite ($MA_4PbI_6 \cdot 2H_2O$).[30,31] And, same as H-MAPbI$_3$ thermochromic perovskite, H-MAPbI$_{3-x}$Cl$_x$ thermochromic perovskite also exhibits the temperature-dependent phase change in the heating and cooling loops, and their XRD patterns at the hot state are both shown in Figure 1c. For H-MAPbI$_3$ thermochromic perovskite, at the hot state, due to the release of water, the dihydrated $MA_4PbI_6 \cdot 2H_2O$ perovskite transforms to the cubic phase of the MAPbI$_3$ perovskite (rhombus symbol in Figure 1c).[32] In Figure 1c, diffraction peaks other than the cubic phase of MAPbI$_3$ can be attributed to the MAI (star symbols), indicating that the thermochromism follows the reaction of cubic phase perovskite, water, and MAI as in Equation (1). These peaks can also be observed in H-MAPbI$_{3-x}$Cl$_x$ thermochromic perovskite patterns, indicating its similar behavior and resultant structure with H-MAPbI$_3$ thermochromic perovskite at the hot state. However, it should be noted that, the typical perovskite (110) peak that appeared at 14.36° for H-MAPbI$_3$ thermochromic perovskite slightly shifted to 14.44° for H-MAPbI$_{3-x}$Cl$_x$ thermochromic perovskite (the inset of Figure 1c). According to Bragg's law,

$$2d \sin\theta = n\lambda \tag{2}$$

the increased θ value corresponds to the decreased d-spacing, correlating to the residual of Cl ions.[33] In summary, the above XRD analysis at the cold and hot states suggests that the Cl$^-$ anion does not alter the crystalline structure too much in H-MAPbI$_{3-x}$Cl$_x$ thermochromic perovskite, and only a small amount of chlorine (Cl) has been incorporated into the final product.

To further investigate the effect of Cl on H-MAPbI$_{3-x}$Cl$_x$ thermochromic perovskite during the synthesizing process, a series of experiments were conducted including the fabrication observations and characterization results. First, during the annealing procedure in the fabrication process, it could be observed that the color of the H-MAPbI$_{3-x}$Cl$_x$ thermochromic perovskite thin film deposited on the glass substrate gradually changes from orange (5 min) to red (30 min), then to dark reddish-brown (60 min) (Figure 1d). The color variation is an important indicator for the chemical reaction during the annealing process. To analyze the bulk concentration of Cl in these three stages, X-ray fluorescence (XRF) was employed on samples annealed at 100 °C for 5, 30, and 60 min, respectively. Figure 1e shows the characteristic X-ray peaks of Pb Mα (2.34 keV), and Cl Kα (2.62 keV) from H-MAPbI$_{3-x}$Cl$_x$ thermochromic perovskite thin films annealed at 100 °C for different time durations. It can be clearly observed that the Cl Kα peak weakens as the annealing time increases, suggesting that Cl gradually escapes from the sample in the form of Cl-containing vapor during the annealing process. To confirm the loss of Cl through Cl vapor during annealing, a blank glass plate was attached to the inner bottom of the petri dish which was placed upside down above the H-MAPbI$_{3-x}$Cl$_x$ thermochromic perovskite samples during the annealing process as shown in Figure S4, Supporting Information. After the H-MAPbI$_{3-x}$Cl$_x$ thermochromic perovskite samples were fully annealed, a deposition of white residue could be observed on the blank glass. The composition of the white residue was analyzed by XRF, and the strong Cl peak is shown in Figure 1f. Note that no Pb and I X-rays can be detected from the glass. This is direct evidence showing the sublimation of Cl-containing vapor during the annealing process. Since the sublimation temperature of MACl is lower than that of MAI, PbCl$_2$, and PbI$_2$,[34] it is possible that the Cl escapes in the form of MACl vapor. The above XRD and XRF analysis clearly suggest that the release of Cl-containing vapor plays an essential role in the formation of H-MAPbI$_{3-x}$Cl$_x$ thermochromic perovskite film.

2.2. Optical Properties of H-MAPbI$_{3-x}$Cl$_x$ Thermochromic Perovskite Smart Windows

Generally, H-MAPbI$_{3-x}$Cl$_x$ TPSW allows the solar irradiance to pass through at the cold state. However, at the hot state, it blocks most of the visible light for saving energy (**Figure 2**a). A scanning electron microscope (SEM) image of an H-MAPbI$_{3-x}$Cl$_x$ film is shown in Figure 2b and the cross-sectional image shows that the thickness of the film is around 1.05 µm. The optical transmittance of the H-MAPbI$_{3-x}$Cl$_x$ TPSW was measured at room temperature (cold state) and 60 °C (hot state) and the results are shown in Figure 2c together with the solar irradiance intensity and photopic luminous efficiency. Figure 2c shows that the thermochromism in H-MAPbI$_{3-x}$Cl$_x$ perovskite primarily tunes the visible light transmittance (380–780 nm), without affecting the infrared transmittance (780–2500 nm).

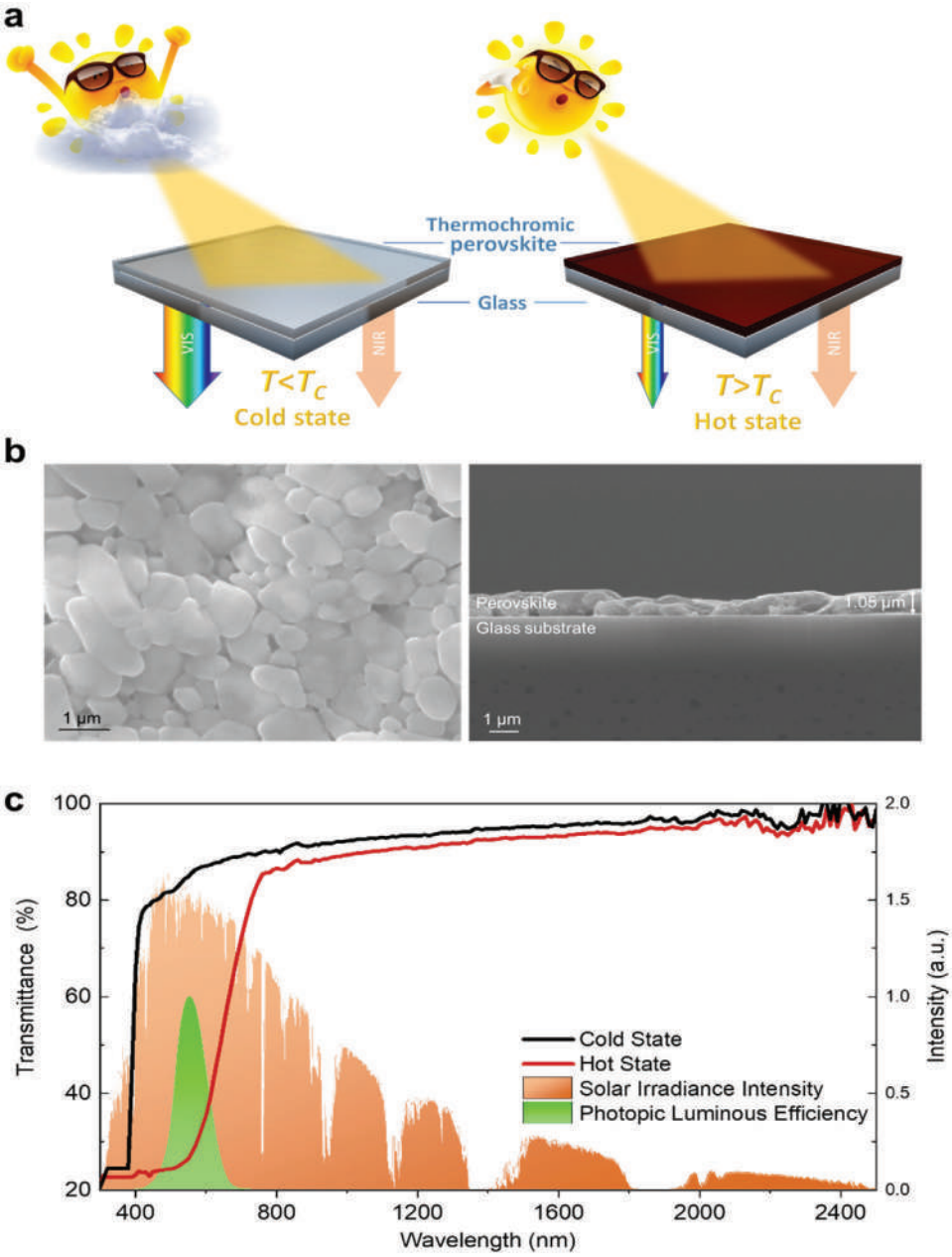

Figure 2. a) Working principle of H-MAPbI$_{3-x}$Cl$_x$ TPSW. b) SEM image of H-MAPbI$_{3-x}$Cl$_x$ thermochromic perovskite thin film. c) Transmittance spectrum of H-MAPbI$_{3-x}$Cl$_x$ TPSW at the cold and hot states.

τ_{lum} of H-MAPbI$_{3-x}$Cl$_x$ at the cold and hot states is 85.2% and 30.3%, respectively. Accordingly, $\Delta\tau_{sol}$ can reach 23.7%. It should be noted that the high $\Delta\tau_{sol}$ can be attributed to the significant difference in the solar transmittance between the cold state and hot state in the ultraviolet and visible light regions, accounting for around 57% of total solar energy in the solar spectrum. The high τ_{lum} at the cold state and high $\Delta\tau_{sol}$ result in its promising optical properties compared with other thermochromic smart windows (e.g., τ_{lum} and $\Delta\tau_{sol}$ of vanadium dioxide (VO_2) thermochromic smart windows are normally ≈50% and ≈10% respectively[35]). **Table 1** compares the optical performance of the H-MAPbI$_{3-x}$Cl$_x$ and the H-MAPbI$_3$ TPSWs. Since the Cl content in the H-MAPbI$_{3-x}$Cl$_x$ is low, it is not surprising that its optical performance is very similar to H-MAPbI$_3$. However, we found that the dilute Cl doping in the H-MAPbI$_{3-x}$Cl$_x$ results in

Table 1. The optical performance comparison between the H-MAPbI$_3$ and H-MAPbI$_{3-x}$Cl$_x$ TPSW.

	$\tau_{lum,hot}$ [%]	$\tau_{lum,cold}$ [%]	$\Delta\tau_{sol}$ [%]
H-MAPbI$_3$ TPSW (MAI:PbI$_2$ = 4:1)	37.4	85.4	23.1
H-MAPbI$_{3-x}$Cl$_x$ TPSW (MAI:PbCl$_2$ = 6.5:1)	30.3	85.2	23.7

a dramatic improvement in transition properties (discussed in the next section).

2.3. Transition Properties of H-MAPbI$_{3-x}$Cl$_x$ TPSW

Apart from the comparable optical properties, H-MAPbI$_{3-x}$Cl$_x$ TPSW also showed a remarkable improvement in transition properties when compared to H-MAPbI$_3$ TPSW. In order to characterize T_c and ΔT_c, the transmittance at 550 nm as a function of temperature for the heating and cooling cycles of the two TPSWs was measured under the ambient condition of 25 °C and *RH* 50% as shown in **Figure 3**a, and $T_{c,h}$, $T_{c,c}$ as well as ΔT_c were calculated accordingly. As the largest transmittance difference of thermochromic perovskites is observed at the wavelength of 550 nm (Figure 2c), which is also the peak in CIE photopic luminous efficiency of the human eye, the transmittance at the wavelength of 550 nm was selected to monitor the thermochromism. It should be noted that to show the relative difference between the two TPSWs, the transmittance intensities shown in Figure 3a are just the relative values rather than absolute figures. The results reveal the $T_{c,h}$ and $T_{c,c}$ of the H-MAPbI$_3$ TPSW to be 53.2 and 30.3 °C, respectively. However, the $T_{c,h}$ of the H-MAPbI$_{3-x}$Cl$_x$ TPSW shows a significant reduction of 8.3 to 44.9 °C compared to the H-MAPbI$_3$ TPSW, and an increase of 5 to 35.3 °C in the cooling process. Most importantly, a much narrower ΔT_c of 9.6 °C is achieved by the H-MAPbI$_{3-x}$Cl$_x$ TPSW, which is significantly lower than that of 22.9 °C obtained by the H-MAPbI$_3$ TPSW. Such a narrow width can be comparable with tungsten doped VO_2 thermochromic smart windows (i.e., 9.4 °C).[36] It can also be seen from Figure 3a that the transmittance of H-MAPbI$_{3-x}$Cl$_x$ TPSW changes quite gradually with the temperature. In contrast, the H-MAPbI$_3$ TPSW undergoes an abrupt and distinct transmittance conversion within 2 °C of temperature change. Indeed, the gradual change of transmittance is a desirable property for a smart window so that light transmittance can be gradually controlled with temperature, instead of only fully colored state and totally transparent state.[37]

As discussed above, the thermochromic effect of H-MAPbI$_{3-x}$Cl$_x$ is caused by the hydration and dehydration processes, implying that the humidity level of the ambient environment is crucial to the transition properties. To further investigate the humidity effect on transition properties of H-MAPbI$_{3-x}$Cl$_x$ TPSW, its $T_{c,h}$, $T_{c,c}$, and ΔT_c were measured under various *RH* conditions and the results are shown in Figure 3b. It can be seen that the $T_{c,h}$ and $T_{c,c}$ both increase with the increase in humidity of the environment, and the average T_c between the heating and cooling processes increases from 29.4 to 51.4 °C. To explain that, during the heating cycle, the high humidity hinders the water molecules escaping from the thermochromic perovskite film, and hence a higher temperature is required to boost the dehydration process. However, in the cooling cycle under high humidity conditions, the water molecules can be more easily absorbed by the thermochromic perovskite even at the high temperature, so that at a *RH* of 80%, we observe a $T_{c,h}$ and $T_{c,c}$ of 54 and 46 °C, respectively. When the *RH* decreases to 25%, the $T_{c,h}$ and $T_{c,c}$ of the H-MAPbI$_{3-x}$Cl$_x$ TPSW are 35.5 and 22.3 °C, respectively. The

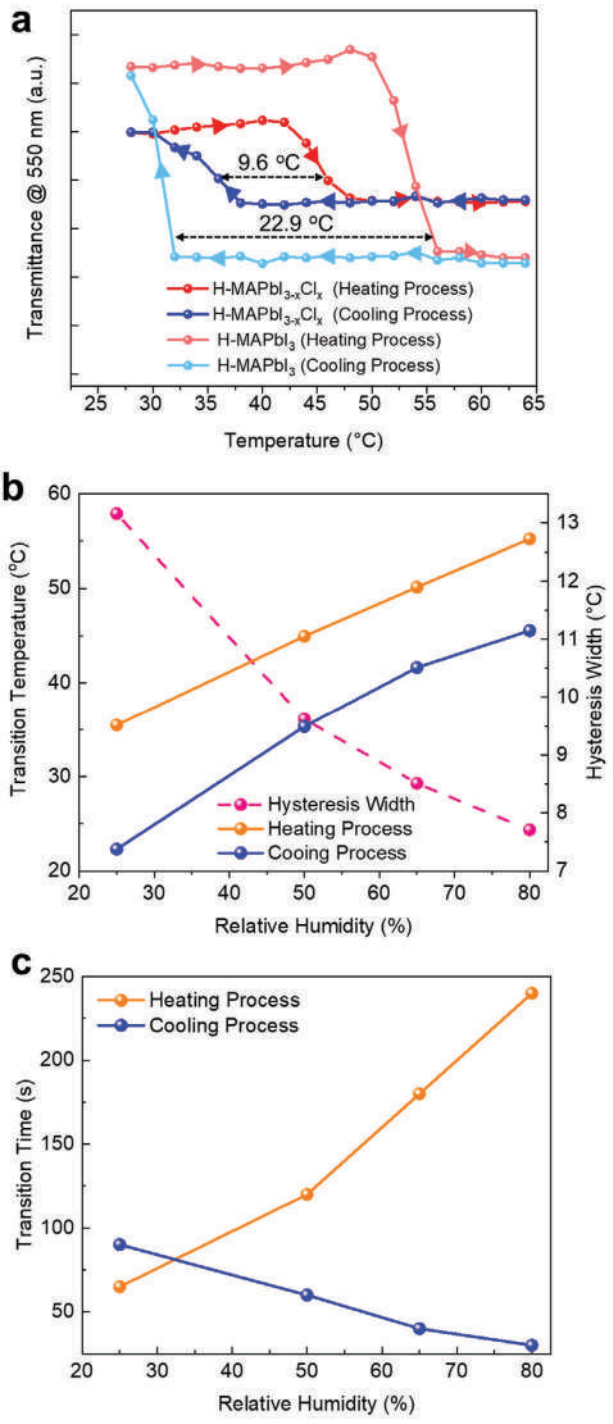

Figure 3. a) The temperature-dependent thermochromic hysteresis loops of the H-MAPbI$_{3-x}$Cl$_x$ and H-MAPbI$_3$ TPSWs upon heating and cooling processes (optical transmittance at 550 nm as a function of temperature). b) Effect of *RH* on the T_c and ΔT_c of the H-MAPbI$_{3-x}$Cl$_x$ TPSW. c) Effect of *RH* on the t_c of the H-MAPbI$_{3-x}$Cl$_x$ TPSW upon heating and cooling processes.

average T_c upon the heating and cooling loops can be as low as 29.4 °C, which is lower than the T_c of other thermochromic smart windows, such as poly(*N*-isopropylacrylmide) hydrogel (e.g., T_c =32 °C). Such a low T_c has never been achieved by

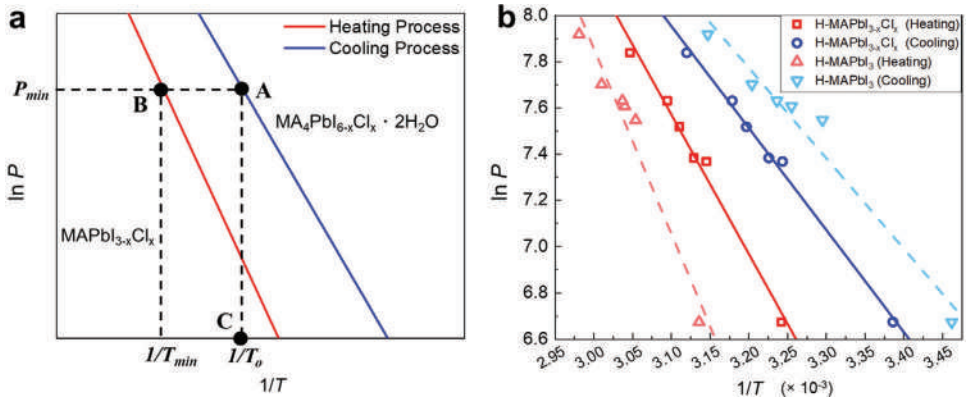

Figure 4. a) Pressure–temperature dependent transition model of thermochromic perovskite in the Clausius–Clapeyron diagram. b) Measurement points upon transition temperature and water vapor pressure of H-MAPbI$_{3-x}$Cl$_x$ and H-MAPbI$_3$ thermochromic perovskites as well as the fitted curve in the Clausius–Clapeyron diagram (solid and dash lines, respectively).

thermochromic perovskite materials before, and this low T_c makes perovskite materials useful as practical smart window coatings. Regarding the effect on the hysteresis width, opposite to that on the transition temperatures, a negative correlation between the ΔT_c of H-MAPbI$_{3-x}$Cl$_x$ thermochromic perovskite and humidity was found as shown by the dash line in Figure 3b. With the increase of humidity level, the hysteresis width decreases from 13.1 to 7.7 °C as the increase of humidity hinders the dehydration while promoting moisture absorption.

As temperature fluctuates during the day, rapid response, namely a short transition time (t_c), is crucial for thermochromic materials in practical applications. Even though there is no strict requirement, an acceptable transition time should be in several minutes for energy efficient smart windows.[10] The t_c in the heating and cooling cycles of the H-MAPbI$_{3-x}$Cl$_x$ thermochromic perovskite was investigated under *RH* ranging from 25% to 80%, corresponding to the measurement of T_c. The results in Figure 3c reflect the humidity dependence of t_c in both heating and cooling processes. With the increase of *RH*, the t_c in the heating process drastically increases from 60 (*RH* = 25%) to 240 s (*RH* = 80%). However, the opposite trend can be observed in the cooling process, where the t_c can be reduced to even lower than 30 s when the *RH* increases to 80%. When the *RH* is 50%, H-MAPbI$_{3-x}$Cl$_x$ shows shorter t_c than H-MAPbI$_3$ TPSW in both heating (120 s vs 240 s) and cooling processes (60 s vs 90 s), proving the enhancement in transition properties.

From the above analysis, a close relationship can be found between humidity (partial water pressure in the air) and transition properties on H-MAPbI$_{3-x}$Cl$_x$ TPSWs. To further quantitatively analyze the reversible dihydrated perovskite formation and dissociation process of H-MAPbI$_{3-x}$Cl$_x$ thermochromic perovskite in relation to humidity, a thermodynamic model is developed. The thermodynamics of hydration and dehydration can be explained by the Clausius–Clapeyron (C–C) relation that reveals the relationship between pressure and temperature in the phase transition boundary (Equation (3)).[38,39] The solution of the C–C relation is shown in Equation (4).

$$A(s) \leftrightarrow B(s) + xC(g) \tag{3}$$

$$\Delta G(T) = \Delta G^0(T) + xRT \ln \frac{p(T)}{p_o} = 0 \tag{4}$$

where ΔG is the molar Gibbs energy change of the reaction, p_o is a reference pressure, ΔG^o is the Gibbs energy change at p_o, and R the gas constant (R=8.314 J mol^{-1} K^{-1}). Considering that $\Delta G^o = \Delta H^o - T\Delta S^o$, where H represents enthalpy and S is entropy, the relationship between pressure and temperature is clearly demonstrated in Equation (5).

$$\ln \frac{p(T)}{p_0} = -\left(\frac{\Delta H^0}{xR}\right)\left(\frac{1}{T}\right) + \frac{\Delta S^0(T)}{xR} \tag{5}$$

According to the C–C relationship, the partial water pressure-transition temperature dependence of the dehydration and hydration process between $MA_4PbI_{6-x}Cl_x \cdot 2H_2O$ and $MAPbI_{3-x}Cl_x$ can be drawn in the C–C diagram as shown in **Figure 4**a, where the red line represents the dehydration process (heating process) and the blue line represents the hydration process (cooling process). The hysteresis width is shown as the area of pseudo-equilibrium between the hydration and dehydration. The thermochromism takes place at a certain temperature T when another parameter (e.g., water vapor pressure P) is fixed. The dotted line from point A to point B demonstrates an isobaric transition from the transparent state ($MA_4PbI_{6-x}Cl_x \cdot 2H_2O$) to the colored state ($MAPbI_{3-x}Cl_x$), that requires a minimum temperature T_{min}, namely the transition temperature of the heating process. Similarly, the line from point C to point A illustrates the isothermal transition from the semitransparent state to the transparent state at room temperature (T_o) by controlling the water vapor pressure. To verify the model, the transition temperatures of H-MAPbI$_{3-x}$Cl$_x$ thermochromic perovskite in the heating and cooling processes were measured at various partial water vapor pressure conditions as shown in Figure 4b. The measured data points in the heating and cooling processes can be well fitted by the linear regression model $\ln P = -6030.2\left(\frac{1}{T}\right) + 26.3$ (red solid line) and $\ln P = -4408.1\left(\frac{1}{T}\right) + 21.6$ (blue solid line), respectively. Through the model, the transition temperature of H-MAPbI$_{3-x}$Cl$_x$ thermochromic perovskite can be easily estimated. This model provides the feasibility to customize the transition temperature of TPSW. In practical

applications, the thermochromic perovskite could be coated at the inner face of a conventional double-glazed window, and by modifying the humidity (the required humidity can be conveniently calculated based on the model) of the air gap in the double-glazed system, the customized transition temperature for the TPSW can be easily achieved. It should be noted that the model is also suitable for H-MAPbI$_3$ thermochromic perovskite as shown in Figure 4b.

2.4. Cycle Performance Test of the H-MAPbI$_{3-x}$Cl$_x$ TPSW

After characterizing the optical and transition properties of H-MAPbI$_{3-x}$Cl$_x$ TPSW, the cycle performance was investigated to ensure its applicability in smart window applications, where the capability of performing stable thermochromism over substantial cycles of heating and cooling processes is expected. A cycle test was conducted on H-MAPbI$_{3-x}$Cl$_x$ TPSW with a total of 50 cooling and heating cycles. The heating and cooling operations were conducted in an air enthalpy testing laboratory (±0.1 °C and ±3% *RH* of error) where the ambient temperature was set at a constant 25 °C with a *RH* of about 50%. It should be noted that in smart window applications, extreme environmental conditions barely occur so that the window temperature is mostly within the normal range (i.e., from room temperature to around 50 °C),[40] thus the heating and cooling temperatures in the cycle test were set as 60 and 25 °C, respectively. During the heating and cooling cycles, the fast and reversible transition between the transparent state (i.e., cold state) and reddish-brown state (i.e., hot state) was consistently displayed throughout the cycle test. Regarding the cycling optical performance, the τ_{lum} at both the hot and cold states of the H-MAPbI$_{3-x}$Cl$_x$ TPSW was detected at five-cycle intervals, using the method as described in Characterization (Experimental Section). **Figure 5**a illustrates the optical property test results, in which the τ_{lum} of the H-MAPbI$_{3-x}$Cl$_x$ TPSW at both the hot and cold states remained almost unchanged over the 50 cycles, resulting in a stable $\Delta\tau_{sol}$. As for the transition properties, the T_c at both the hot and cold states of the H-MAPbI$_{3-x}$Cl$_x$ TPSW was recorded at 10-cycle intervals. Figure 5b shows the transition property test results, in which the sample demonstrated nearly the same transition temperature at both the hot and cold states over the 50 cycles, contributing to the constant hysteresis width. The cycle test results strongly indicate that the H-MAPbI$_{3-x}$Cl$_x$ TPSW has the ability to undergo substantial heating and cooling cycles while maintaining the stable and promising thermochromic performance.

2.5. Model House Field Test

To test the energy saving performance of this H-MAPbI$_{3-x}$Cl$_x$ TPSW, a field test using a model house was conducted in the early autumn of Hong Kong (weather information is shown in Table S1, Supporting Information). Two glass pieces (each 9 cm × 9 cm) were sealed together to build a double-glazed window (**Figure 6**a) and the perovskite film was coated on the inner faces of the windows. The H-MAPbI$_{3-x}$Cl$_x$ TPSW was installed on a heat-insulated acrylic model house (Model House 1) with the volume of 20 × 20 × 20 cm^3. Another model house (Model House 2) with a quartz glass double-glazed window (Figure S5, Supporting Information) was also constructed as a reference for comparison. The experimental setup is shown in Figure 6b and the field test was conducted on the rooftop of a building. The windows of the model houses faced the sky to mimic the roof window. Two thermocouples (T-type) were utilized to monitor the indoor air temperature and window temperature, respectively. The ambient temperature and global solar irradiation were measured by a weather station. The test results are shown in Figure 6c. After sunrise (7:00 AM), the indoor air temperature increased rapidly with the increase of solar intensity. The indoor air temperature of Model House 1 equipped with the H-MAPbI$_{3-x}$Cl$_x$ TPSW was lower than that of Model House 2 during the daytime, which confirms the sunlight shielding effect induced by the H-MAPbI$_{3-x}$Cl$_x$ TPSW. The largest indoor air temperature reduction of 3.5 °C was achieved in Model House 1 at 1:00 PM. It should be noted that the temperature of the H-MAPbI$_{3-x}$Cl$_x$ TPSW in Model House 1 was always higher than the quartz glass window in Model House 2, but the indoor air temperature of Model House 1 was lower than that of Model House 2, implying that the direct solar

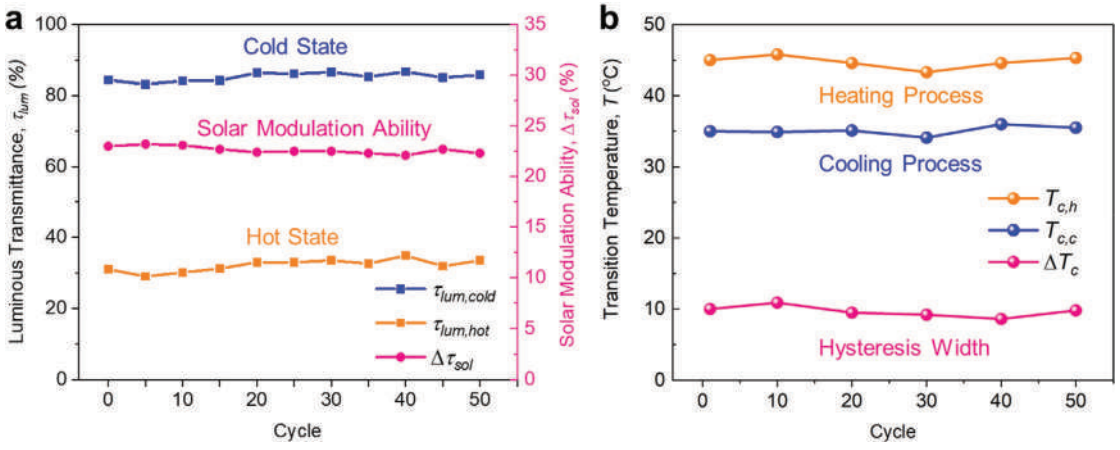

Figure 5. a) Optical performance ($\tau_{lum,hot}$, $\tau_{lum,cold}$, and $\Delta\tau_{sol}$) of the H-MAPbI$_{3-x}$Cl$_x$ TPSW after 50 cycles. b) Transition properties ($T_{c,h}$, $T_{c,c}$, and ΔT_c) of the H-MAPbI$_{3-x}$Cl$_x$ TPSW after 50 cycles.

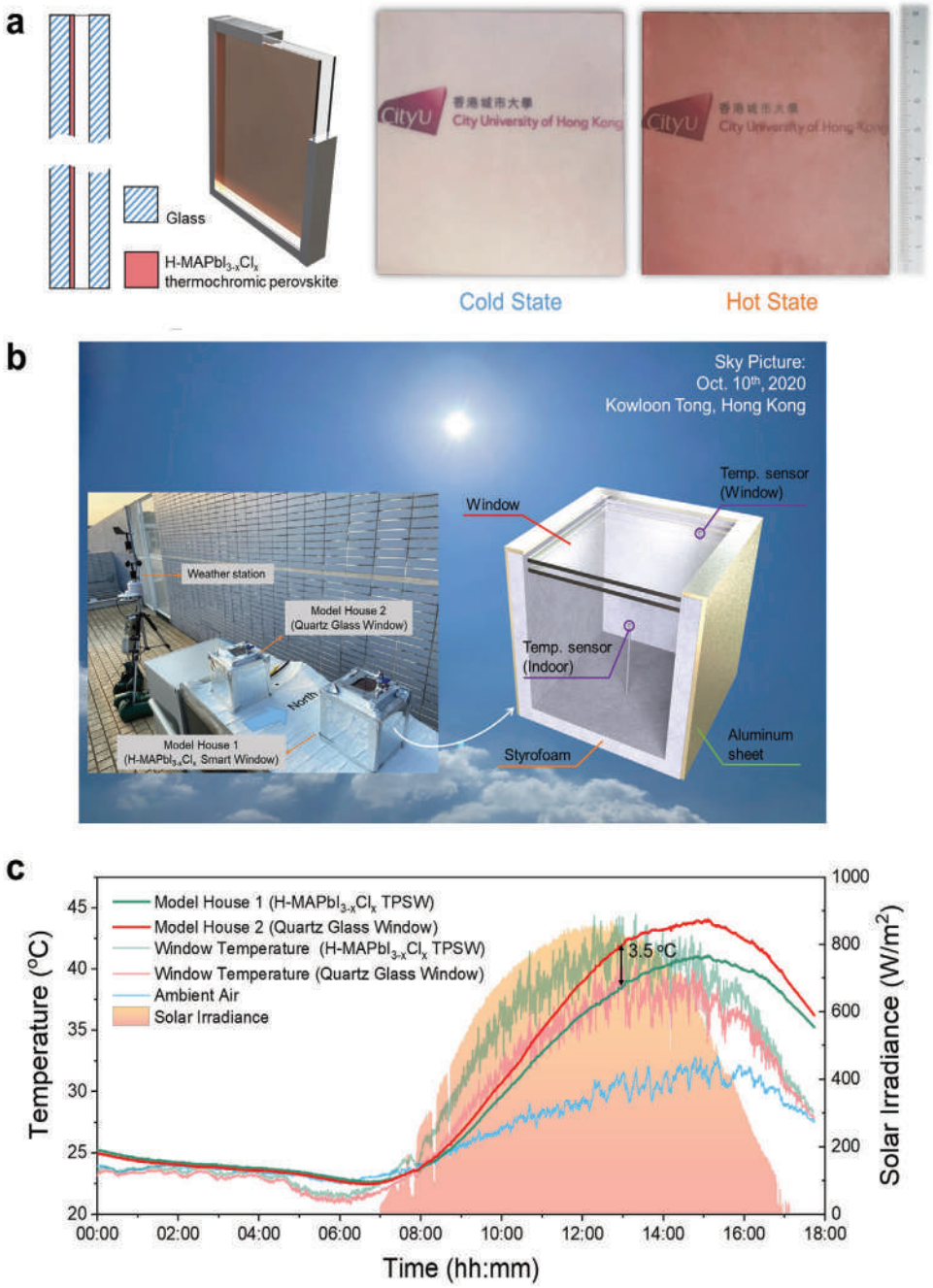

Figure 6. a) Schematics of the double-glazed H-MAPbI$_{3-x}$Cl$_x$ TPSW and the 9 cm × 9 cm glass at the cold and hot states for the model house field test. b) Scheme of model house field test set up. c) 18 h temperature curve for the model house field test on the 10th October, 2020 in Hong Kong.

radiation is the dominant factor to heat the indoor environment rather than heat conduction between the window and indoor air. Furthermore, when the solar intensity decreased in the late afternoon, the indoor air temperature difference between the two model houses gradually reduced, because H-MAPbI$_{3-x}$Cl$_x$ TPSW mainly mitigates energy loss/gain through modulating the solar radiation. It should be noted that the field test was conducted in the autumn in Hong Kong where the highest solar irradiance is only ≈860 W m^{-2}. It is expected that the indoor air temperature reduction can be larger in summer when the solar irradiance exceeds 1000 W m^{-2}. Overall, the field test results prove that the H-MAPbI$_{3-x}$Cl$_x$ TPSW can effectively block the solar radiation, demonstrating great potential as smart windows in building applications.

2.6. Comparisons with Previous Studies

To further demonstrate the improved optical and thermochromic performance of the H-MAPbI$_{3-x}$Cl$_x$ TPSW in this

Table 2. Optical and transition properties comparison of various thermochromic smart windows.

Categories	Materials/methods	Optical properties				Transition properties						Refs.
		$\tau_{lum,hot}$ [%]	$\tau_{lum,cold}$ [%]	τ_{lum} [%]	$\Delta\tau_{sol}$ [%]	$T_{c,h}$ [°C]	$T_{c,c}$ [°C]	T_c [°C]	ΔT_c [°C]	$t_{c,h}$ [s]	$t_{c,c}$ [s]	
Perovskite smart windows	H-$MAPbI_3$	37.4	85.4	61.4	23.1	53.2	30.3	41.8	22.9	240	90	[31]
	H-$MAPbI_{3-x}Cl_x$	30.3	85.2	57.8	23.7	44.9	35.3	40.1	9.6	120	60	This study
	$MAPbI_3{\bullet}xCH_3NH_2$	3.0	68.0	35.5	-	-	-	-	-	220	180	[25]
	$CsPbI_{3-x}Br_x$	35.4	81.7	58.6	-	150.0	-	-	-	In hours	-	[24]
Hydrogel smart windows	PNIPAm	59.9	87.9	73.9	20.4	-	-	32.0	-	-	-	[42]
	HPC	48.7	86.1	67.4	25.7	-	-	38.0	-	-	-	[43]
	PNVCL	-	-	88.0	-	34.0	25.0	28.0	9.0	60	150	[44]
VO_2 smart windows	Chemical doping	62.0	68.4	65.2	7.9	-	-	30.5	9.4	-	-	[36]
	Polymer-assisted deposition	39.9	43.3	41.6	14.1	-	-	-	-	-	-	[45]
	Bio-inspired moth eye	45.3	43.6	44.5	7.1	-	-	-	-	-	-	[46]
Nickel (II) iodide smart windows[a)]	Nickel (II) iodide	10.7	87.5	49.1	63.5	53	29.5	41.3	23.5			[41]

[a)]The optical and transition properties were calculated based on the figures presented in ref. [41].

study, an inclusive comparison with other related works, such as perovskite, hydrogel, VO_2, and nickel (II) iodide thermochromic smart windows, is presented in **Table 2**. For various thermochromic smart windows, several different materials or synthesizing methods were included with the references of published works. The optical and transition properties were considered for evaluation in terms of the smart window performance.

Among perovskite materials, the H-$MAPbI_{3-x}Cl_x$ TPSW shows comparatively high average τ_{lum} and $\Delta\tau_{sol}$. Most importantly, it exhibits the shortest transition time for both heating and cooling processes, and the hysteresis width is even half that of the similar H-$MAPbI_3$ TPSW. Compared with the hydrogel thermochromic smart window, the optical properties of the studied H-$MAPbI_{3-x}Cl_x$ are still comparable, while the risk of liquid leakage of the hydrogel thermochromic smart window can be eliminated since the H-$MAPbI_{3-x}Cl_x$ thermochromic perovskite is a thin film deposited on the glass. With regard to the VO_2 thermochromic smart window, because optical regulation only occurs in the near infrared region, the average $\Delta\tau_{sol}$ of VO_2 is only half that of the studied H-$MAPbI_{3-x}Cl_x$ TPSW. At the cold state, unlike the transparent H-$MAPbI_{3-x}Cl_x$ TPSW, the VO_2 thermochromic smart windows are brownish in color, and therefore provide less visual clarity for building occupants. In addition, a nickel (II) Iodide based thermochromic smart window was recently proposed that possesses relatively high optical modulation ability, and yet the hysteresis width was still large.[41] Overall, H-$MAPbI_{3-x}Cl_x$ TPSW provides outstanding thermochromic properties compared with different thermochromic smart windows. Most importantly, a great reduction in hysteresis width is also achieved by the H-$MAPbI_{3-x}Cl_x$ TPSW, making it more suitable in real applications.

3. Conclusion

In this study, a novel H-$MAPbI_{3-x}Cl_x$ thermochromic perovskite is proposed as a material for smart windows with its thermochromism achieved by the manipulated phase transitions between dihydrated perovskite (low-temperature) and perovskite (high-temperature) phases. It demonstrates highly reversible color change during heating and cooling processes with a transmittance record of τ_{lum} = 85.2% and 30.3% at the cold and hot states, respectively. The significant transmittance contrast in the visible light region leads to a high $\Delta\tau_{sol}$ of 23.7%. EDS, XRD, and XRF measurements show that only a small amount of Cl remains in the fully annealed perovskite films. By monitoring the annealing process and analyzing the released vapor product, it is found that the formation of the H-$MAPbI_{3-x}Cl_x$ thermochromic perovskite is likely driven by the release of gaseous MACl (or other organic chloride compounds). Furthermore, due to the existence of a small amount of Cl, the H-$MAPbI_{3-x}Cl_x$ thermochromic perovskite shows remarkable transition properties compared with H-$MAPbI_3$ thermochromic perovskite, namely, a much lower T_c (29.4–51.4 °C) and narrower ΔT_c (7.7–13.2 °C) as well as a shorter t_c (1–4 min) could be achieved by controlling the humidity of the environment. Furthermore, using the obtained data, we developed a thermodynamic model which can easily predict the T_c of H-$MAPbI_{3-x}Cl_x$ thermochromic perovskite at different *RH* conditions. Most importantly, a 3.5 °C indoor air temperature reduction was achieved in a field test using a model house equipped with the H-$MAPbI_{3-x}Cl_x$ TPSW, showing a promising energy saving potential compared with conventional windows. However, it should be pointed out that, similar to perovskite solar cells, the long-term stability of H-$MAPbI_{3-x}Cl_x$ thermochromic perovskite should be further comprehensively studied. In summary, H-$MAPbI_{3-x}Cl_x$ TPSW presents advanced optical performance and delivers an alternative method to further improve the transition properties of thermochromic perovskite materials, opening up a new research direction to develop high performance thermochromic smart windows.

4. Experimental Section

Materials and Chemicals: CH_3NH_3I (MAI, 99.5%) was supplied from Xi'an Polymer Light Technology. $PbCl_2$ (99%) and PbI_2 (99%) were

provided by Sigma Aldrich. DMF (≥99.5%) was purchased from Alfa Aesar.

Fabrication of Smart Windows: The sample fabrication was conducted in a glovebox (water content ≤ 1 ppm, oxygen content ≤ 1 ppm). Noted that two groups of samples were fabricated: H-MAPbI$_{3-x}$Cl$_x$ thermochromic perovskite synthesized by MAI and $PbCl_2$ in different molar ratio of 6.5:1, and H-MAPbI$_3$ thermochromic perovskite synthesized by MAI and PbI_2 in the molar ratio of 4:1. Perovskite precursor solution was prepared by the one-step deposition process. More specifically, 6.5 M MAI and 1 M $PbCl_2$, or 4 M MAI and 1 M PbI_2 were dissolved in DMF solvent, respectively and then vigorously stirred at 50 °C until the solute was completely dissolved and the solution was absolutely clear. Quartz glass substrates were cleaned with detergent, then ethanol and then deionized water in an ultrasonic bath for 10 min, respectively. The cleaned substrates were then air-dried and treated in UV ozone cleaner for 15 min to improve surface wettability.[47] Perovskite thin film was spin-coated on the treated surface of the substrates, with a certain amount of the precursor, at 2000 rpm for 30 s. Then the 6.5MAI:1$PbCl_2$ and 4MAI:1PbI_2 coated thin films were immediately annealed on a hot plate at 100 °C for 1 h and 15 min, respectively, to evaporate the residual solvents and facilitate crystallization.[48]

Characterization: All characterization processes were conducted under an ambient condition. Crystal structure was characterized by XRD (XRD PANalytical). Elemental composition was measured by XRF Spectrometer (S2 PUMA Series 2, Bruker) by monitoring the Cl (K), I (L), and Pb (M) characteristic X-ray lines. The measurement of FTIR spectrum was conducted by SHIMADZU IRAffinity 1 spectrometer. The perovskite precursor was spin coated on the silicon wafer, and attenuated total reflectance mode was used to scan the spectrum. EDS was conducted by Hitachi S4800 Field Emission SEM. Luminous transmission was characterized by a UV–vis–NIR spectrophotometer from 300 to 2500 nm (Lambda 950, Perkin Elmer equipped with an integrating sphere detector, USA). A temperature controller (including a heater, a T-type thermocouple, and a Digi-sense TC9600 temperature controller) was attached to modulate the temperature of the sample in order to measure the transmission at both cold state (25 °C) and hot state (60 °C). The amount of transmitted visible light and solar radiation could be quantified by calculating luminous transmittance τ_{lum} $\left(\tau_{lum}=\frac{\int_{\lambda=380nm}^{780nm}\overline{y}(\lambda)\tau(\lambda)d\lambda}{\int_{\lambda=380nm}^{780nm}\overline{y}(\lambda)d\lambda}\right)$ and solar transmittance τ_{sol} $\left(\tau_{sol}=\frac{\int_{\lambda=300nm}^{2500nm}AM_{1.5}(\lambda)\tau(\lambda)d\lambda}{\int_{\lambda=300nm}^{2500nm}AM_{1.5}(\lambda)d\lambda}\right)$. Then the $\Delta\tau_{sol}$ could also be calculated as $\Delta\tau_{sol}=\tau_{sol}^{cold}-\tau_{sol}^{hot}$, where $\tau(\lambda)$ is the transmittance of the windows at wavelength λ. $\overline{y}(\lambda)$ is the photopic luminous efficiency of the human eye defined by the CIE (International Commission on Illumination) standard, and $AM_{1.5}(\lambda)$ is the solar irradiance spectrum for an absolute air mass of 1.5 which is known as the reference or standard spectra. A wavelength range 300 nm ≤ λ ≤ 2500 nm was chosen which accounted for 99.2% of terrestrial solar energy.[49] For the transition temperature measurement (T_c), the experiments were conducted at an air enthalpy testing laboratory where the temperature and *RH* could be controlled at constant set values and the experiment setup is shown in Figure S6, Supporting Information. More specifically, four groups of experiments were carried out, under 25%, 50%, 65%, and 80% *RH*, while keeping the room temperature constant at 25 °C. For each level of humidity, the samples were heated on a hot plate from room temperature to 60 °C and then cooled back to 20 °C by a tailor-made electronic cooling plate, at intervals of 2 °C. The samples were kept on the hot/cooling plate for 2 min to ensure the stability of the color. Simultaneously, under each temperature, the visible light transmittance of the samples was measured using Lens Transmission meter (SDR8508) at 550 nm wavelength. T_c was determined by plotting the first derivative of the transmittance to the temperature as a function of temperature, and the T_c is the temperature showing the minimum value at the first derivative.

Supporting Information

Supporting Information is available from the Wiley Online Library or from the author.

Acknowledgements

This project was funded by Hong Kong Research Grant Council (RGC) via General Research Fund (GRF) account 16200518 and Collaborative Research Fund (CRF) account C6022-16G as well as City University of Hong Kong StartUp Fund and SRG Fund via the accounts of 9610411 and 7005579, respectively.

Conflict of Interest

The authors declare no conflict of interest.

Data Availability Statement

Data available on request from the authors.

Keywords

energy-efficient buildings, perovskite, smart windows, solar modulation, thermochromism

Received: December 4, 2020
Revised: February 23, 2021
Published online: March 26, 2021

[1] M. Kamalisarvestani, R. Saidur, S. Mekhilef, F. S. Javadi, *Renewable Sustainable Energy Rev.* **2013**, *26*, 353.
[2] S. Liu, C. Y. Tso, H. H. Lee, Y. Zhang, K. M. Yu, C. Y. H. Chao, *Sci. Rep.* **2020**, *10*, 1.
[3] H. Ye, X. Meng, B. Xu, *Energy Build.* **2012**, *49*, 164.
[4] H. Y. Lee, Y. Cai, S. Bi, Y. N. Liang, Y. Song, X. M. Hu, *ACS Appl. Mater. Interfaces* **2017**, *9*, 6054.
[5] A. Taylor, I. Parkin, N. Noor, C. Tummeltshammer, M. S. Brown, I. Papakonstantinou, *Opt. Express* **2013**, *21*, A750.
[6] L. Long, H. Ye, *Sci. Rep.* **2014**, *4*, 6427.
[7] T. G. La, X. Li, A. Kumar, Y. Fu, S. Yang, H. J. Chung, *ACS Appl. Mater. Interfaces* **2017**, *9*, 33100.
[8] K. Li, S. Meng, S. Xia, X. Ren, G. Gao, *ACS Appl. Mater. Interfaces* **2020**, *12*, 42193.
[9] Y. Ke, J. Chen, G. Lin, S. Wang, Y. Zhou, J. Yin, P. S. Lee, Y. Long, *Adv. Energy Mater.* **2019**, *9*, 1902066.
[10] Y. Ke, C. Zhou, Y. Zhou, S. Wang, S. H. Chan, Y. Long, *Adv. Funct. Mater.* **2018**, *28*, 1800113.
[11] G. Hamaoui, N. Horny, C. L. Gomez-Heredia, J. A. Ramirez-Rincon, J. Ordonez-Miranda, C. Champeaux, F. Dumas-Bouchiat, J. J. Alvarado-Gil, Y. Ezzahri, K. Joulain, M. Chirtoc, *Sci. Rep.* **2019**, *9*, 8728.
[12] J. B. Kana Kana, J. M. Ndjaka, G. Vignaud, A. Gibaud, M. Maaza, *Opt. Commun.* **2011**, *284*, 807.
[13] L. Hu, H. Tao, G. Chen, R. Pan, M. Wan, D. Xiong, X. Zhao, *J. Sol-Gel Sci. Technol.* **2016**, *77*, 85.
[14] S. Long, X. Cao, G. Sun, N. Li, T. Chang, Z. Shao, P. Jin, *Appl. Surf. Sci.* **2018**, *441*, 764.

[15] M. Saliba, J. P. Correa-Baena, C. M. Wolff, M. Stolterfoht, N. Phung, S. Albrecht, D. Neher, A. Abate, *Chem. Mater.* **2018**, *30*, 4193.
[16] F. Zhou, Z. Ren, Y. Zhao, X. Shen, A. Wang, Y. Y. Li, C. Surya, Y. Chai, *ACS Nano* **2016**, *10*, 5900.
[17] K. Yang, F. Li, J. Zhang, C. P. Veeramalai, T. Guo, *Nanotechnology* **2016**, *27*, 095202.
[18] W. Zhang, M. Anaya, G. Lozano, M. E. Calvo, M. B. Johnston, H. Míguez, H. J. Snaith, *Nano Lett.* **2015**, *15*, 1698.
[19] A. E. Shalan, S. Kazim, S. Ahmad, *ChemSusChem* **2019**, *12*, 4116.
[20] N. G. Park, *Mater. Today* **2015**, *18*, 65.
[21] M. Batmunkh, Y. L. Zhong, H. Zhao, *Adv. Mater.* **2020**, *32*, 2000631.
[22] N. K. Noel, S. D. Stranks, A. Abate, C. Wehrenfennig, S. Guarnera, A. A. Haghighirad, A. Sadhanala, G. E. Eperon, S. K. Pathak, M. B. Johnston, A. Petrozza, L. M. Herz, H. J. Snaith, *Energy Environ. Sci.* **2014**, *7*, 3061.
[23] L. Shen, H. lap Yip, F. Gao, L. Ding, *Sci. Bull.* **2020**, *65*, 980.
[24] J. Lin, M. Lai, L. Dou, C. S. Kley, H. Chen, F. Peng, J. Sun, D. Lu, S. A. Hawks, C. Xie, F. Cui, A. P. Alivisatos, D. T. Limmer, P. Yang, *Nat. Mater.* **2018**, *17*, 261.
[25] L. M. Wheeler, D. T. Moore, R. Ihly, N. J. Stanton, E. M. Miller, R. C. Tenent, J. L. Blackburn, N. R. Neale, *Nat. Commun.* **2017**, *8*, 1.
[26] P. G. Kusalik, D. Bergman, A. Laaksonen, *J. Chem. Phys.* **2000**, *113*, 8036.
[27] M. De Bastiani, M. I. Saidaminov, I. Dursun, L. Sinatra, W. Peng, U. Buttner, O. F. Mohammed, O. M. Bakr, *Chem. Mater.* **2017**, *29*, 3367.
[28] B. A. Rosales, L. E. Mundt, T. G. Allen, D. T. Moore, K. J. Prince, C. A. Wolden, G. Rumbles, L. T. Schelhas, L. M. Wheeler, *Nat. Commun.* **2020**, *11*, 5234.
[29] S. K. Sharma, C. Phadnis, T. K. Das, A. Kumar, B. Kavaipatti, A. Chowdhury, A. Yella, *Chem. Mater.* **2019**, *31*, 3111.
[30] A. Halder, D. Choudhury, S. Ghosh, A. S. Subbiah, S. K. Sarkar, *J. Phys. Chem. Lett.* **2015**, *6*, 3180.
[31] Y. Zhang, C. Y. Tso, J. S. Iñigo, S. Liu, H. Miyazaki, C. Y. H. Chao, K. M. Yu, *Appl. Energy* **2019**, *254*, 113690.
[32] T. Baikie, Y. Fang, J. M. Kadro, M. Schreyer, F. Wei, S. G. Mhaisalkar, M. Graetzel, T. J. White, *J. Mater. Chem. A* **2013**, *1*, 5628.
[33] R. Cheng, C. C. Chung, H. Zhang, F. Liu, W. T. Wang, Z. Zhou, S. Wang, A. B. Djurišić, S. P. Feng, *Adv. Energy Mater.* **2019**, *9*, 1901980.
[34] A. Dualeh, P. Gao, S. Il Seok, M. K. Nazeeruddin, M. Grätzel, *Chem. Mater.* **2014**, *26*, 6160.
[35] Y. Cui, Y. Ke, C. Liu, Z. Chen, N. Wang, L. Zhang, Y. Zhou, S. Wang, Y. Gao, Y. Long, *Joule* **2018**, *2*, 1707.
[36] M. Kong, K. Egbo, C. P. Liu, M. K. Hossain, C. Y. Tso, C. Y. Hang Chao, K. M. Yu, *J. Alloys Compd.* **2020**, *833*, 155053.
[37] H. Y. Lee, Y. Cai, S. Velioglu, C. Mu, C. J. Chang, Y. L. Chen, Y. Song, J. W. Chew, X. M. Hu, *Chem. Mater.* **2017**, *29*, 6947.
[38] E. R. T. Bevers, P. J. Van Ekeren, W. G. Haije, H. A. J. Oonk, *J. Therm. Anal. Calorim.* **2006**, *86*, 825.
[39] Y. A. Chang, W. A. Oates, *Materials Thermodynamics*, Wiley, New York, UK **2010**, p. 318.
[40] L. Long, H. Ye, H. Zhang, Y. Gao, *Sol. Energy* **2015**, *120*, 55.
[41] T. D. Siegler, L. C. Reimnitz, M. Suri, S. H. Cho, A. J. Bergerud, M. K. Abney, D. J. Milliron, B. A. Korgel, *Langmuir* **2019**, *35*, 2146.
[42] Y. Zhou, Y. Cai, X. Hu, Y. Long, *J. Mater. Chem. A* **2014**, *2*, 13550.
[43] Y. S. Yang, Y. Zhou, F. B. Yin Chiang, Y. Long, *RSC Adv.* **2016**, *6*, 61449.
[44] R. L. Sala, R. H. Gonçalves, E. R. Camargo, E. R. Leite, *Sol. Energy Mater. Sol. Cells* **2018**, *186*, 266.
[45] L. Kang, Y. Gao, H. Luo, Z. Chen, J. Du, Z. Zhang, *ACS Appl. Mater. Interfaces* **2011**, *3*, 135.
[46] X. Qian, N. Wang, Y. Li, J. Zhang, Z. Xu, Y. Long, *Langmuir* **2014**, *30*, 10766.
[47] P. Kuang, K. Constant, in *Wetting and Wettability*, InTechOpen, London, UK **2015**, pp. 85–103.
[48] Z. Xiao, Q. Dong, C. Bi, Y. Shao, Y. Yuan, J. Huang, *Adv. Mater.* **2014**, *26*, 6503.
[49] C. Liu, I. Balin, S. Magdassi, I. Abdulhalim, Y. Long, *Opt. Express* **2015**, *23*, A124.